

# Strongly Coupled Spin Waves and Surface Acoustic Waves at Room Temperature

Yunyoung Hwang<sup>1,2</sup>, Jorge Puebla<sup>2,\*</sup>, Kouta Kondou<sup>2</sup>, Carlos Gonzalez-Ballester<sup>3,4</sup>, Hironari Isshiki<sup>1</sup>, Carlos Sánchez Muñoz<sup>5</sup>, Liyang Liao<sup>1</sup>, Fa Chen<sup>6</sup>, Wei Luo<sup>6</sup>, Sadamichi Maekawa<sup>2,7,8</sup>, and Yoshichika Otani<sup>1,2,†</sup>

<sup>1</sup>*Institute for Solid State Physics, University of Tokyo, Kashiwa 277-8581, Japan*

<sup>2</sup>*Center for Emergent Matter Science, RIKEN, Wako-shi, Saitama, 351-0198, Japan*

<sup>3</sup>*Institute for Quantum Optics and Quantum Information of the Austrian Academy of Sciences, A-6020 Innsbruck, Austria*

<sup>4</sup>*Institute for Theoretical Physics, University of Innsbruck, A-6020 Innsbruck, Austria*

<sup>5</sup>*Departamento de Física Teórica de la Materia Condensada and Condensed Matter Physics Center (IFIMAC), Universidad Autónoma de Madrid, 28049 Madrid, Spain*

<sup>6</sup>*School of Integrated Circuits, Wuhan National Laboratory for Optoelectronics, Huazhong University of Science and Technology, Wuhan 430074, People's Republic of China*

<sup>7</sup>*Advanced Science Research Center, Japan Atomic Energy Agency, Tokai 319-1195, Japan*

<sup>8</sup>*Kavli Institute for Theoretical Sciences, University of Chinese Academy of Sciences, Beijing 100049, People's Republic of China*



(Received 15 September 2023; revised 6 November 2023; accepted 15 December 2023; published 31 January 2024)

Here, we report the observation of strong coupling between magnons and surface acoustic wave (SAW) phonons in a thin CoFeB film constructed in an on-chip SAW resonator by analyzing SAW phonon dispersion anticrossings. We employ a nanostructured SAW resonator design that, in contrast to conventional SAW resonators, allows us to enhance shear-horizontal strain. Crucially, this type of strain couples strongly to magnons. Our device design provides the tunability of the film thickness with a fixed phonon wavelength, which is a departure from the conventional approach in strong magnon-phonon coupling research. We detect a monotonic increase in the coupling strength by expanding the film thickness, which agrees with our theoretical model. Our work offers a significant way to advance fundamental research and the development of devices based on magnon-phonon hybrid quasiparticles.

DOI: [10.1103/PhysRevLett.132.056704](https://doi.org/10.1103/PhysRevLett.132.056704)

Hybridization between two systems can be characterized by a comparison of the coupling strength  $g$  and the relaxation rates of each system  $\kappa_1$  and  $\kappa_2$ . When  $g/\max(\kappa_1, \kappa_2) > 1$ , the hybridized state is in the strong coupling regime [1]. In the case of coupling of magnons and other waves, reducing the magnon relaxation rate is experimentally challenging, thus increasing  $g$  is the most efficient route to realize strong coupling. The most straightforward approach to achieve higher coupling strength is increasing the number of spins coupled in phase to the desired mode [1]. This approach is typically done for magnons coupling to photons in cavity magnonics experiments by increasing the volume of the magnet [2]. The rationale behind this approach lies in the relatively spatially homogeneous microwave cavity modes throughout the magnet, especially for magnets significantly smaller than the microwave wavelength ( $\sim$ mm).

However, in the context of magnon-phonon coupling research, this approach is not always straightforward as the magnon and phonon are not necessarily in phase across the sample, and thus the magnon-phonon coupling depends nontrivially on the sample geometry. For instance, in a spherical magnet, the magnon-phonon coupling decreases with the volume [3–5]. Nonetheless, one can circumvent this apparent limitation by choosing an appropriate geometry for the magnetic medium: a thin film with a much

smaller thickness than the involved acoustic wavelength. Since it supports spatially uniform spin and acoustic waves across the film thickness, the coupling strength recovers its characteristic monotonic increase with the expansion of the film thickness. Hence, the thin film limit allows us to explore the dependence of magnon-phonon coupling on the number of spins. In order to make it possible, it is crucial to attain independent control over the phonon wavelengths and the geometry of the magnetic material.

Several studies demonstrated magnon-phonon coupling [6–9], and some studies experimentally observed strong magnon-phonon coupling [10–13]. However, the strong dependence of the phonon wavelength on the dimensionality of the active magnetic layer within the structure [7,9,11,12] imposes limitations on the ability to separately control the phonon wavelength and the size of the magnet, hindering the realization of the thin film limit. One viable approach to accomplish this limit is **injecting surface acoustic waves (SAWs) with variable wavelengths into the magnetic material** as has been researched over the past two decades [14–25]. Especially, Refs. [20,23] employed a two-port SAW resonator that consists of SAW generation and detection devices enclosed by distributed Bragg reflectorlike stripes, forming an acoustic cavity [26,27]. This device design allows driving acoustic modes with any

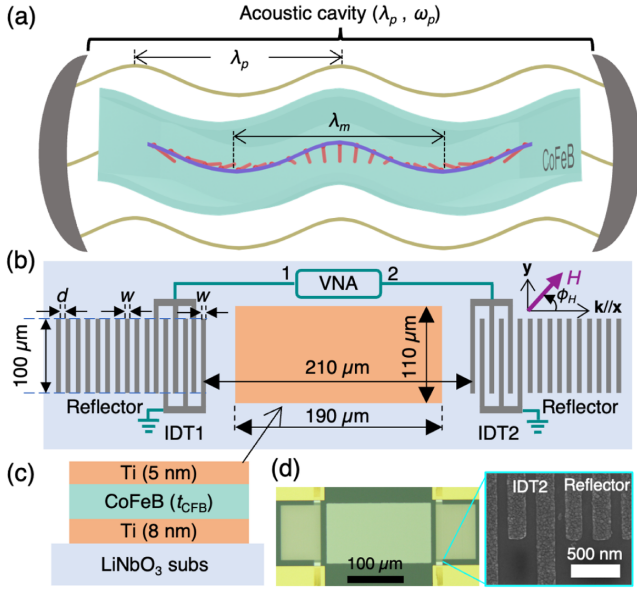


FIG. 1. (a) Schematic illustration of strong magnon-phonon coupling in an acoustic cavity that confines phonons with a wavelength  $\lambda_p$  and a frequency  $\omega_p$ . The yellow curves denote acoustic waves (phonons) created within the acoustic cavity and the red arrows represent magnetization dynamics. The phonons propagating through a CoFeB thin film excite a spin wave (magnon), which is represented by the purple curve, with a matched wavelength  $\lambda_m = \lambda_p$ . (b) Schematic top view of the device structure used in this research. IDT1 and IDT2 include 20 pairs of Al stripes and each set of reflectors includes 200 Al stripes. IDT1 and IDT2 are respectively connected to port1 and port2 of a vector network analyzer (VNA). (c) Schematic side view of the Ti/CFB/Ti stack. (d) Optical (left) and scanning electron microscope (right) images of one of the devices used in this study.

wavelength  $\lambda_p$  (frequency  $\omega_p$ ) enabling coupling to magnons at the wavelength  $\lambda_m = \lambda_p$  by spin wave resonance (SWR), as depicted in Fig. 1(a), circumventing the reliance of  $\lambda_p$  on the material geometry. However, despite successfully reduced phonon loss and enhanced coupling strength using acoustic cavities, strong coupling between magnons and SAW phonons was not achieved [20,23]. This is because experiments on the coupling between magnons and SAW phonons mostly utilize Rayleigh-SAWs, which exhibit limited magnetoelastic coupling into the film thickness direction, limiting the attainable coupling strength [22]. On the contrary, shear-horizontal (SH)-SAWs enable a significantly stronger magnetoelastic coupling through a magnetic film, thus efficiently having a larger coupling strength [22].

In this Letter, we demonstrate the strong coupling between magnons and SH-SAW phonons caused by SAW-driven SWR in a Co<sub>20</sub>Fe<sub>60</sub>B<sub>20</sub> (CFB) thin film on a 128° Y-cut LiNbO<sub>3</sub> (128-LN) substrate at room temperature by measuring anticrossing of SAW phonon dispersion, an indication of strong interaction [28]. We generate SAWs

using a nanostructured high-frequency acoustic cavity significantly smaller than previous reports in the field [20,23]. The anticrossing behavior is only detected when the angle between the SAW propagation and an applied in-plane magnetic field,  $\phi_H$ , is around 0°. In contrast, the previous results that utilized acoustic cavity structures [20,23] detect magnon-phonon coupling only at  $\phi_H \sim 45^\circ$ , consistent with the behavior of SWR driven by SH- and Rayleigh-SAWs, respectively [15,22], confirming that our device corresponds to the former. Despite the smaller contribution of SH-SAWs compared to Rayleigh-SAWs on 128-LN [29–32], the improved mechanical coupling between SH- and Rayleigh-SAWs within the well-defined periodic gratings of our acoustic cavity led to an enhancement of SH-SAWs [33,34]. Furthermore, by the realized thin film limit as mentioned, we successfully estimated the magnon-phonon coupling strength ( $g$  values) of samples with the same device structure but varying CFB thicknesses ( $t_{\text{CFB}}$ ) by fitting the observed anticrossing with our theoretical model. Our study reveals a monotonic increase in  $g$  with increasing  $t_{\text{CFB}}$ , which agrees with our expectation and our magnon-phonon coupling model. This increase of  $g$  allowed us to achieve strong coupling;  $g/\max(\kappa_m, \kappa_p) > 1$ , where  $\kappa_{m(p)}$  is the magnon (phonon) relaxation rate, for devices with  $t_{\text{CFB}} \geq 20$  nm.

To generate SAWs, we utilized interdigital transducers (IDTs) that can generate and detect SAWs on a piezoelectric substrate [26]. We fabricated acoustic cavity devices including Ti(8 nm)/CFB( $t_{\text{CFB}}$ )/Ti(5 nm) layers on a 128-LN substrate, as shown in Figs. 1(b) and 1(c), where the parameters inside the parentheses exhibit the thickness of each layer. For the IDTs and the acoustic reflectors, we deposited 35-nm-thick Al. Each Al stripe of an IDT has a length of 120  $\mu\text{m}$  and a width of  $w$ . Each Al stripe of the acoustic reflectors has a length of 100  $\mu\text{m}$  and the same width as the IDT stripes,  $w$ . All metallic stripes of the IDTs and the acoustic reflectors are separated by a distance  $d$ . The scanning electron microscope image in Fig. 1(d) shows the measured values of  $w$  and  $d$ :  $w = 175 \pm 8$  nm; and  $d = 125 \pm 4$  nm. After the fabrication of the acoustic cavity, we patterned a 190  $\mu\text{m} \times 110 \mu\text{m}$  rectangle between the two IDTs. The Ti/CFB/Ti layers are sputter-deposited to the rectangle pattern. We fabricated samples with the same structure but different  $t_{\text{CFB}} = 10, 20, 25, 30$ , and 35 nm.

SAW transmission ( $|S_{21}|^2$ ) is measured using a vector network analyzer (VNA) while applying an external in-plane magnetic field  $H$ , where the angle between  $H$  and the SAW wave vector  $\mathbf{k}$  is described by  $\phi_H$ . This transmission is shown in Fig. 1(b). When  $H$  is far enough from the resonant field of SWR driven by our SAW frequency, the SAW spectrum shows the phonon signal without contributions from magnons, which remain unexcited. Such a situation is shown in Fig. 2(a), which depicts  $|S_{21}|^2$  of the sample with  $t_{\text{CFB}} = 20$  nm out of magnetic resonance when

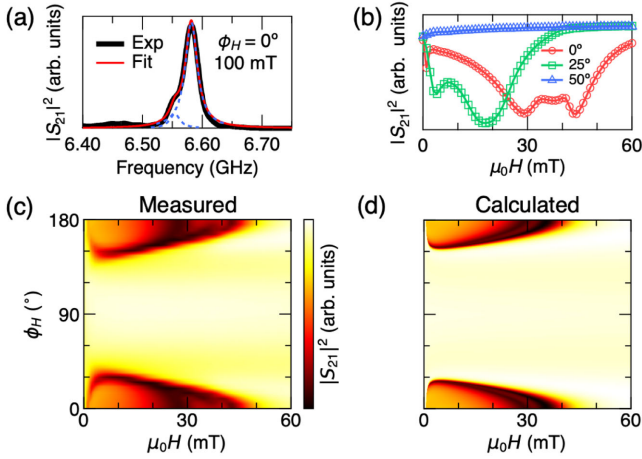


FIG. 2. SAW measurement results of the sample  $t_{\text{CFB}} = 20$  nm. (a) Measured SAW transmission signal ( $|S_{21}|^2$ ) by VNA in the frequency domain. An in-plane magnetic field of 100 mT is externally applied in a direction parallel to the SAW propagation, which is far from the resonant field of SWR driven by our SAW frequency as shown in (b), thus the transmission signal displays only the phonon response. The black curve exhibits the measured spectrum, and the red curve shows the multiple Lorentzian fitting. The blue dashed curves show the individual Lorentzian peaks of the fitting. (b)  $|S_{21}|^2$  at the frequency of 6.58 GHz as a function of the amplitude of the externally applied in-plane magnetic field ( $\mu_0 H$ ). The in-plane field angles ( $\phi_H$ ) of each curve are shown in the legend. (c)  $|S_{21}|^2$  at the frequency of 6.58 GHz as a function of  $\mu_0 H$  and  $\phi_H$ . (d) Calculated SAW transmission with the same setup as (c).

$\mu_0 H = 100$  mT and  $\phi_H = 0^\circ$ . The resonant frequency of the strongest SAW peak is  $f_r = 6.58$  GHz. The designed wavelength of the SAW ( $\lambda_r$ ) is determined by the designed structure of our acoustic device;  $\lambda_r = 2(w + d) = 600$  nm. Using these parameters, one can calculate the SAW velocity as  $v = f_r \lambda_r = 3,950$  m/s. This value aligns with the typical SAW velocity propagating on the crystal  $x$  axis of 128-LN [35].

In addition to the main resonance, we found one more peak on the lower frequency side of the main resonance [see the fitting to two Lorentzian peaks in the blue dashed curves in Fig. 2(a)]. The presence of these two peaks originates from the existence of two modes allowed within our cavity device. A detailed explanation of the origin of the two SAW peaks can be found in Sec. 1 of Ref. [36]. This Lorentzian fitting is used to extract the phonon linewidth  $\delta_p$  to estimate the phonon relaxation rate below.

The SAW transmission out of magnetic resonance decreases when  $H$  approaches the resonance field condition since the phonons are used to excite magnons [14,15,19,20,41]. Figure 2(b) shows the absorption of  $|S_{21}|^2$  of the main SAW peak in Fig. 2(a) when  $\phi_H = 0^\circ$ ,  $25^\circ$ , and  $50^\circ$ . Figure 2(c) shows  $|S_{21}|^2$  as a function of  $\mu_0 H$  and  $\phi_H$ . In the case of a typical magnetoelastic coupling excited by a Rayleigh-SAW, the absorption amplitude shows

maximum when  $\phi_H = 45^\circ$  [14,15,19–21,25,37,41,42]. However, our results indicate that the maximum absorption across all  $\phi_H$  ranges at  $\phi_H \sim 25^\circ$  and no absorption was detected when  $\phi_H > 30^\circ$ . This is because the magnon dispersion is raised to a higher frequency due to the dipolar field and does not meet the phonon dispersion at  $\phi_H > 30^\circ$  (Fig. 8 of Ref. [36]). Note that the in-plane uniaxial magnetic anisotropy of our CFB film [43] aligned in-plane perpendicular to  $\mathbf{k}$  causes the dips of SAW transmission around  $\mu_0 H = 0$ . Assuming the uniaxial magnetic anisotropy and the magnon-phonon coupling strength obtained by experiments (see below) allow us to calculate the SAW transmission as a function of an external in-plane magnetic field. As shown in Fig. 2(d), the calculation agrees well with the measured result. A detailed description of the calculation can be found in Sec. 5A of Ref. [36].

The distinct observation of anticrossing, represented by split features in SAW absorption, becomes most pronounced when  $\phi_H \sim 0^\circ$ . This splitting does not originate from Rayleigh-SAWs, commonly considered the dominant one in SAWs generated on a 128-LN substrate, which show the maximum magnetoelastic coupling when the angle between  $\mathbf{k}$  and the magnetization, described as  $\phi$ , is  $45^\circ$  and no magnetoelastic coupling when  $\phi = 0^\circ$ . On the other hand, SH-SAWs show the maximum magnetoelastic coupling when  $\phi = 0^\circ$  or  $90^\circ$  [15]. While in our device, the strain of Rayleigh-SAW,  $\epsilon_{xx}$ , is larger than that of SH-SAW,  $\epsilon_{xy}$  (Fig. 2(c) of Ref. [36]), and  $\epsilon_{xx}$  decreases abruptly away from the surface [22]. Therefore,  $\epsilon_{xx}$  faces a limitation in terms of penetration depth, which results in an insufficient coupling strength to observe magnon-phonon anticrossing. On the contrary,  $\epsilon_{xy}$  has a larger penetration depth, making the associated coupling strength dominant [22].

Having clarified the origin of the coupling, we now focus on the magnon-phonon coupling at  $\phi_H = 0^\circ$ , where the magnetoelastic coupling is dominated by SH-SAW. Figure 3(a) shows the SAW transmission signal  $|S_{21}|^2$  of the sample with  $t_{\text{CFB}} = 10$  nm as a function of frequency and  $\mu_0 H$ , and Fig. 3(b) the SAW transmission spectrum when  $\mu_0 H = 100$  mT. As we mentioned above, a SAW peak exists at a lower frequency side to the main peak, giving rise to multiple anticrossing features. However, as each SAW mode couples only to the magnon mode with its same wave number, each SAW branch shows a single anticrossing. Therefore, we focus on anticrossing of one mode per device to estimate its coupling. We first fit the phonon branches in  $\omega$ - $H$  dispersion taken by the local maximum of the SAW spectrum [see the marker in Fig. 3(b)] at each field with our magnon-phonon coupling model:

$$\omega^2 = \frac{\omega_m^2 + \omega_p^2}{2} \pm \frac{1}{2} \sqrt{(\omega_m^2 - \omega_p^2)^2 + (2\delta\omega_{\text{bare}}^2)^2}, \quad (1)$$

where  $\omega_m$  and  $\omega_p$  are the magnon and phonon resonant frequencies. The derivation of Eq. (1) and the definition of



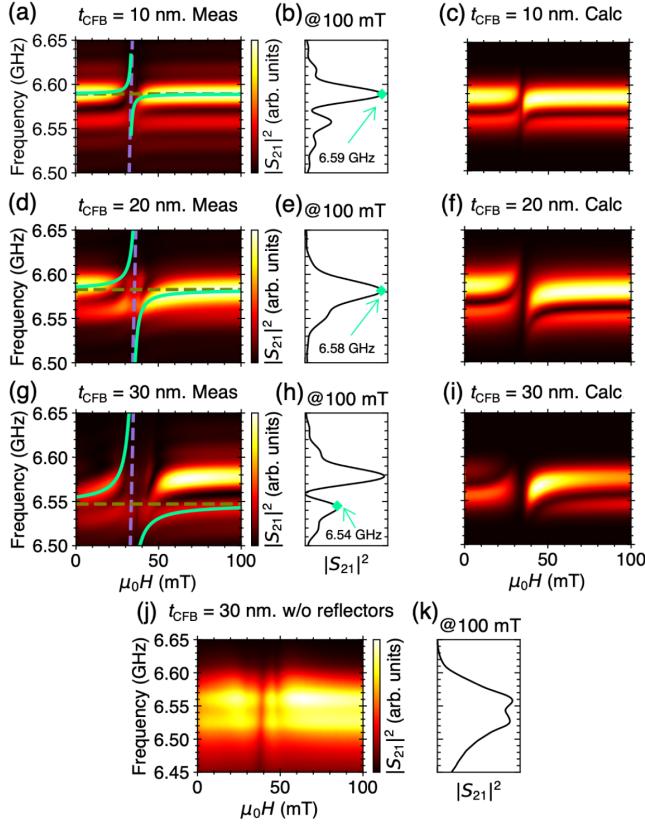


FIG. 3. SAW transmissions when the external magnetic field is applied in the direction of SAW propagation;  $\phi_H = 0^\circ$ . (a),(b) SAW transmission signal ( $|S_{21}|^2$ ) of the sample with  $t_{\text{CFB}} = 10$  nm under (a) various amplitudes of the magnetic field  $\mu_0 H$  and (b)  $\mu_0 H = 100$  mT. The green marker in (b) represents the local maximum used for the anticrossing fitting, shown as the green curves in (a). (c) Calculated SAW transmission of the sample with  $t_{\text{CFB}} = 10$  nm as a function of the frequency and  $\mu_0 H$ . (d)–(i) Same as (a)–(c), but measurements and calculations of the samples with (d)–(f)  $t_{\text{CFB}} = 20$  nm and (g)–(i)  $t_{\text{CFB}} = 30$  nm. (j),(k)  $|S_{21}|^2$  of the sample with  $t_{\text{CFB}} = 30$  nm, but in the absence of acoustic reflectors (j) under various  $\mu_0 H$  and (k)  $\mu_0 H = 100$  mT. The purple and khaki dashed curves in (a), (d), and (g) indicate the calculated magnon (SWR) and phonon dispersions, respectively, as Fig. 8(a) of Ref. [36].

$\delta\omega_{\text{bare}}$  can be found in Sec. 4 of Ref. [36]. The anticrossing fitting is shown in Fig. 3(a) as green curves. The design of our SAW devices fixes the wave number  $k = 2\pi/\lambda_r$ , precluding the direct characterization of the  $\omega$ – $k$  dispersion; however, a schematic of the  $\omega$ – $k$  dispersion indicating the working area of our device can be found in Fig. 6 of Ref. [36].

From the parameters obtained by the fitting, we reproduce the anticrossing detected by SAW transmission spectra using our SAW transmission model. We modeled two phonon modes coupling to each magnon mode corresponding to its wave number. For the details of the model, see Sec. 5 of Ref. [36]. As a result, the SAW transmission is well reproduced as shown in Fig. 3(c).

Furthermore, in Figs. 3(d)–3(i), we present the same analysis as shown in Figs. 3(a)–3(c) but for the samples with  $t_{\text{CFB}} = 20$  and 30 nm. Especially for the sample with  $t_{\text{CFB}} = 30$  nm, it is notable that the upper phonon branch of the main SAW peak in Fig. 3(g) is vaguely visible at  $\mu_0 H \sim 0$ ; however, it is no longer detectable at  $0 < \mu_0 H < 40$  mT, as this peak shifts out of the frequency range of our cavity due to a redshift given by the strong mode interaction. Therefore, we fitted anticrossing of the peak at 6.54 GHz in Fig. 3(h) to obtain the parameters as shown in Fig. 3(g). The results and calculations of samples with other  $t_{\text{CFB}}$  are shown in Fig. 9 of Ref. [36].

Additionally, a device with the same structure as used in this experiment but without the presence of the acoustic reflectors does not show any anticrossing as shown in Figs. 3(j) and 3(k). This is due to the considerably higher phonon relaxation and smaller coupling strength originating from smaller SH-SAW when there is an absence of reflectors that form an acoustic cavity (Secs. 2 and 3B of Ref. [36]). The reason for the significant enhancement of SH-SAWs by the presence of acoustic cavity is the mechanical scattering of Rayleigh-SAW into SH-SAW within the periodic gratings of our acoustic cavity [33,34].

Lastly, we present the magnon-phonon coupling estimation in the devices with varying CFB thicknesses. Figure 4(a) shows the coupling strength  $g$  as a function of  $t_{\text{CFB}}$  taken by the anticrossing fittings in Fig. 3 and Fig. 9 of Ref. [36] with Eq. (1) and Eqs. (9), (12) of Ref. [36]. While our magnon-phonon coupling model (Sec. 4 of Ref. [36]) predicts  $g \sim \sqrt{t_{\text{CFB}}}$ , this prediction does not hold true, as shown in Fig. 4(a), due to variations in the effective magnetoelastic coupling coefficient  $b$  with changes in the thickness of the ferromagnetic layer. It is known that  $b$  is determined by contributions of the bulk ( $b_v$ ) and surface ( $b_s$ ) magnetoelastic couplings [44–46] as  $b = b_v + b_s/t_{\text{CFB}}$ . Figure 4(b) shows  $b$  as a function of the inverse of  $t_{\text{CFB}}$ , determined by the values of  $g$  and Eq. (12) of Ref. [36].

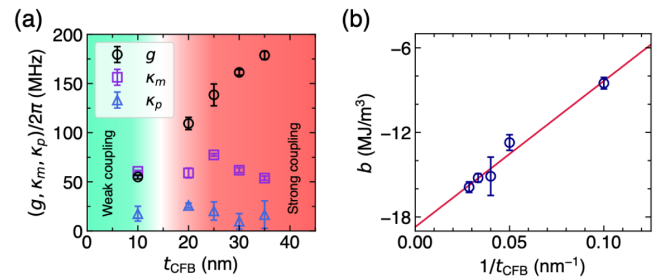


FIG. 4. (a) The coupling strength ( $g$ , the black curve) and magnon ( $\kappa_m$ , the purple square) and phonon ( $\kappa_p$ , the blue triangle) relaxation rates as a function of the thickness of the CFB layer. (b) The effective magnetoelastic constant as a function of the inverse of the thickness of the CFB layer. The solid line exhibits the surface magnetoelastic coupling fitting. The data points and error bars of (a) and (b) are the mean and s.d. of measurements of three or more different devices, respectively.

The fitting of  $b$  with the surface magnetoelastic coupling shown as a solid line yields  $b_v = -18.7 \text{ MJ/m}^3$  and  $b_s = 104 \text{ mJ/m}^2$ , where the values are in agreement with the known values for CFB [46].

Next, to evaluate the attainment of strong coupling we estimate the relaxation rates of magnons ( $\kappa_m$ ) and phonons ( $\kappa_p$ ). To obtain  $\kappa_m$ , we used the Gilbert damping  $\alpha$  of our CFB films as  $\kappa_m = \omega_m \alpha$ . The Gilbert damping is measured by ferromagnetic resonance using coplanar waveguides (see Sec. 6 and Fig. 10 of Ref. [36]). For  $\kappa_p$ , we obtain the linewidth of  $|S_{21}|^2$  peaks ( $\delta_p$ ) by Lorentzian fittings as shown as the dashed curves in Fig. 2(a) and determine  $\kappa_p = 2\pi\delta_p$ . The estimated relaxation rates of devices with varying  $t_{\text{CFB}}$  are depicted alongside the coupling strength in Fig. 4(a). For the devices with  $t_{\text{CFB}} \geq 20 \text{ nm}$ ,  $g > \kappa_m, \kappa_p$ , i.e., strong coupling is achieved. However, for the devices with  $t_{\text{CFB}} = 10 \text{ nm}$ ,  $\kappa_m > g$ , thus it is not in the strong coupling regime.

To summarize, we achieved strong coupling between magnons and SAW phonons in  $\text{Co}_{20}\text{Fe}_{60}\text{B}_{20}$  thin films thanks to the use of an acoustic cavity constructed by a two-port SAW resonator. SAW phonon anticrossings are observed when an external magnetic field is applied parallel to the SAW propagation direction. By fitting anticrossings with our theoretical model, we estimated the coupling strength of our devices. For the devices with  $t_{\text{CFB}} \geq 20 \text{ nm}$ , we confirmed the achievement of strong coupling. The variety in selecting magnetic materials and the usage of well-established SAW devices will pave the way to explore magnon-phonon strong coupling physics with on-chip devices at room temperature. This could be a significant asset toward integrating magnons within GHz-frequency quantum technological platforms, which is currently difficult due to the large wavelength mismatch and resulting weak coupling between microwaves and magnons. Our work offers the potential solution for establishing such couplings via mediating phonons, which have been demonstrated to be efficient interfaces with solid-state qubits [47], superconducting qubits [48,49], and other quantum systems in the GHz domain [50]. Moreover, it holds the potential to offer insights into studying coherently coupled magnon-phonon hybridized quasiparticles [22,51] enabling the development of magnetic field-controlled acoustic devices and less lossy magnon-based information processing devices. Having observed anticrossing through SAW signals, the potential for further advancements, such as magnetoelastic wave detection using techniques like Brillouin light scattering [9,52], is a promising avenue for exploration.

This work was supported by Grants-in-Aid for Scientific Research (S) (No. 19H05629) and the Japan Society for the Promotion of Science Grants-in-Aid for Scientific Research (No. 20H01865). Y. H. thanks to RIKEN Junior Research Associate Program for supporting this work. L. L. would

like to acknowledge the support from JSPS through Research Program for Young Scientists (No. 23KJ0778). F. C. and W. L. acknowledge China National Key Research and Development Plan (2022YFE0103300), and Y. O. acknowledges the LANE Chair of Excellence and QSPIN project at University Grenoble Alpes, and the RIKEN-China cooperation project. The authors thank Kei Yamamoto for fruitful discussions and Machie Kaitou for the help in taking scanning electron microscope images.

\*Corresponding author: jorgeluis.pueblanunez@riken.jp

†Corresponding author: yotani@issp.u-tokyo.ac.jp

- [1] A. F. Kockum, A. Miranowicz, S. De Liberato, S. Savasta, and F. Nori, Ultrastrong coupling between light and matter, *Nat. Rev. Phys.* **1**, 19 (2019).
- [2] Y. Tabuchi, S. Ishino, T. Ishikawa, R. Yamazaki, K. Usami, and Y. Nakamura, Hybridizing ferromagnetic magnons and microwave photons in the quantum limit, *Phys. Rev. Lett.* **113**, 083603 (2014).
- [3] X. Zhang, C.-L. Zou, L. Jiang, and H. X. Tang, Cavity magnomechanics, *Sci. Adv.* **2**, e1501286 (2016).
- [4] C. Gonzalez-Ballester, J. Gieseler, and O. Romero-Isart, Quantum acoustomechanics with a micromagnet, *Phys. Rev. Lett.* **124**, 093602 (2020).
- [5] C. Gonzalez-Ballester, D. Hümmer, J. Gieseler, and O. Romero-Isart, Theory of quantum acoustomagnonics and acoustomechanics with a micromagnet, *Phys. Rev. B* **101**, 125404 (2020).
- [6] H. Man, Z. Shi, G. Xu, Y. Xu, X. Chen, S. Sullivan, J. Zhou, K. Xia, J. Shi, and P. Dai, Direct observation of magnon-phonon coupling in yttrium iron garnet, *Phys. Rev. B* **96**, 100406(R) (2017).
- [7] S. Mondal, M. A. Abeed, K. Dutta, A. De, S. Sahoo, A. Barman, and S. Bandyopadhyay, Hybrid magnetodynamical modes in a single magnetostrictive nanomagnet on a piezoelectric substrate arising from magnetoelastic modulation of precessional dynamics, *ACS Appl. Mater. Interfaces* **10**, 43970 (2018).
- [8] J. Zhang, M. Chen, J. Chen, K. Yamamoto, H. Wang, M. Hamdi, Y. Sun, K. Wagner, W. He, Y. Zhang, J. Ma, P. Gao, X. Han, D. Yu, P. Maletinsky, J.-P. Ansermet, S. Maekawa, D. Grundler, C.-W. Nan, and H. Yu, Long decay length of magnon-polarons in  $\text{BiFeO}_3/\text{La}_{0.67}\text{Sr}_{0.33}\text{MnO}_3$  heterostructures, *Nat. Commun.* **12**, 7258 (2021).
- [9] K. An, C. Kim, K. W. Moon, R. Kohno, G. Olivetti, G. de Loubens, N. Vukadinovic, J. Ben Youssef, C. Hwang, and O. Klein, Optimizing the magnon-phonon cooperativity in planar geometries, *Phys. Rev. Appl.* **20**, 014046 (2023).
- [10] T. Kikkawa, K. Shen, B. Flebus, R. A. Duine, K.-I. Uchida, Z. Qiu, G. E. W. Bauer, and E. Saitoh, Magnon polarons in the spin Seebeck effect, *Phys. Rev. Lett.* **117**, 207203 (2016).
- [11] C. Berk, M. Jaris, W. Yang, S. Dhuey, S. Cabrini, and H. Schmidt, Strongly coupled magnon-phonon dynamics in a single nanomagnet, *Nat. Commun.* **10**, 2652 (2019).
- [12] K. An, A. N. Litvinenko, R. Kohno, A. A. Fuad, V. V. Naletov, L. Vila, U. Ebels, G. De Loubens, H. Hurdequint,

- N. Beaulieu, J. Ben Youssef, N. Vukadinovic, G.E.W. Bauer, A.N. Slavin, V.S. Tiberkevich, and O. Klein, Coherent long-range transfer of angular momentum between magnon Kittel modes by phonons, *Phys. Rev. B* **101**, 060407(R) (2020).
- [13] T. Hioki, Y. Hashimoto, and E. Saitoh, Coherent oscillation between phonons and magnons, *Commun. Phys.* **5**, 115 (2022).
- [14] M. Weiler, L. Dreher, C. Heeg, H. Huebl, R. Gross, M. S. Brandt, and S. T. B. Goennenwein, Elastically driven ferromagnetic resonance in nickel thin films, *Phys. Rev. Lett.* **106**, 117601 (2011).
- [15] L. Dreher, M. Weiler, M. Pernpeintner, H. Huebl, R. Gross, M. S. Brandt, and S. T. B. Goennenwein, Surface acoustic wave driven ferromagnetic resonance in nickel thin films: Theory and experiment, *Phys. Rev. B* **86**, 134415 (2012).
- [16] M. Weiler, H. Huebl, F. S. Goerg, F. D. Czeschka, R. Gross, and S. T. B. Goennenwein, Spin pumping with coherent elastic waves, *Phys. Rev. Lett.* **108**, 176601 (2012).
- [17] D. Labanowski, A. Jung, and S. Salahuddin, Power absorption in acoustically driven ferromagnetic resonance, *Appl. Phys. Lett.* **108**, 022905 (2016).
- [18] X. Li, D. Labanowski, S. Salahuddin, and C. S. Lynch, Spin wave generation by surface acoustic waves, *J. Appl. Phys.* **122**, 043904 (2017).
- [19] M. Xu, J. Puebla, F. Auvray, B. Rana, K. Kondou, and Y. Otani, Inverse Edelstein effect induced by magnon-phonon coupling, *Phys. Rev. B* **97**, 180301(R) (2018).
- [20] Y. Hwang, J. Puebla, M. Xu, A. Lagarrigue, K. Kondou, and Y. Otani, Enhancement of acoustic spin pumping by acoustic distributed Bragg reflector cavity, *Appl. Phys. Lett.* **116**, 252404 (2020).
- [21] M. Xu, K. Yamamoto, J. Puebla, K. Baumgaertl, B. Rana, K. Miura, H. Takahashi, D. Grundler, S. Maekawa, and Y. Otani, Nonreciprocal surface acoustic wave propagation via magneto-rotation coupling, *Sci. Adv.* **6**, eabb1724 (2020).
- [22] N. K. P. Babu, A. Trzaskowska, P. Graczyk, G. Centała, S. Mieszczak, H. Głowiński, M. Zdunek, S. Mielcarek, and J. W. Klos, The interaction between surface acoustic waves and spin waves: The role of anisotropy and spatial profiles of the modes, *Nano Lett.* **21**, 946 (2021).
- [23] D. Hatanaka, M. Asano, H. Okamoto, Y. Kunihashi, H. Sanada, and H. Yamaguchi, On-chip coherent transduction between magnons and acoustic phonons in cavity magnomechanics, *Phys. Rev. Appl.* **17**, 034024 (2022).
- [24] R. Gao, Y. Ye, H. Wu, X. Li, X. Liu, J. Wang, and Q. Liu, Magnetoacoustic waves controlled by in-plane uniaxial magnetic anisotropy, *Appl. Phys. Lett.* **121**, 042401 (2022).
- [25] Y. Hwang, J. Puebla, K. Kondou, and Y. Otani, Voltage signals caused by surface acoustic wave driven ferromagnetic resonance under out-of-plane external fields, *Adv. Mater. Interfaces* **9**, 2201432 (2022).
- [26] D. T. Bell and R. C. M. Li, Surface-acoustic-wave resonators, *Proc. IEEE* **64**, 711 (1976).
- [27] J. Puebla, Y. Hwang, K. Kondou, and Y. Otani, Progress in spinconversion and its connection with band crossing, *Ann. Phys. (Amsterdam)* **534**, 2100398 (2022).
- [28] H. Huebl, C. W. Zollitsch, J. Lotze, F. Hocke, M. Greifenstein, A. Marx, R. Gross, and S. T. B. Goennenwein, High cooperativity in coupled microwave resonator ferromagnetic insulator hybrids, *Phys. Rev. Lett.* **111**, 127003 (2013).
- [29] D. Cullen, G. Meltz, and T. Grudkowski, Surface and interface acoustic waves in  $\text{SiO}_2/\text{YX} - \text{LiNbO}_3$ , *Appl. Phys. Lett.* **44**, 182 (1984).
- [30] T. Nakao, M. Kadota, K. Nishiyama, Y. Nakai, D. Yamato, Y. Ishiura, T. Komura, N. Takada, and R. Kita, Smaller surface acoustic wave duplexer for US personal communication service having good temperature characteristics, *Jpn. J. Appl. Phys.* **46**, 4760 (2007).
- [31] Y. Nakai, T. Nakao, K. Nishiyama, and M. Kadota, Surface acoustic wave duplexer composed of  $\text{SiO}_2$  film with convex and concave on Cu-electrodes/ $\text{LiNbO}_3$  structure, in *Proceedings of the 2008 IEEE Ultrasonics Symposium* (IEEE, San Diego, 2008), p. 1580.
- [32] K.-Y. Hashimoto, M. Kadota, T. Nakao, M. Ueda, M. Miura, H. Nakamura, H. Nakanishi, and K. Suzuki, Recent development of temperature compensated saw devices, in *Proceedings of the 2011 IEEE International Ultrasonics Symposium* (IEEE, Orlando, 2011), p. 79.
- [33] V. Plessky, P. Turner, N. Fenzi, and V. Grigorievsky, Interaction between the Rayleigh-type SAW and the SH-wave in a periodic grating on a  $128^\circ\text{-LN}$  substrate, in *Proceedings of the 2010 IEEE International Ultrasonics Symposium* (IEEE, Beijing, 2010), p. 167.
- [34] B. Zhang, T. Han, G. Tang, Q. Zhang, T. Omori, and K.-Y. Hashimoto, Influence of coupling with shear horizontal surface acoustic wave on lateral propagation of Rayleigh surface acoustic wave on  $128^\circ\text{YX} - \text{LiNbO}_3$ , *Jpn. J. Appl. Phys.* **56**, 07JD02 (2017).
- [35] K. Shibayama, K. Yamanouchi, H. Sato, and T. Meguro, Optimum cut for rotated Y-Cut  $\text{LiNbO}_3$  crystal used as the substrate of acoustic-surface-wave filters, *Proc. IEEE* **64**, 595 (1976).
- [36] See Supplemental Material at <http://link.aps.org/supplemental/10.1103/PhysRevLett.132.056704> for the description of the multiple SAW modes, SAW strain simulations, supplemental measurements to confirm contributions from the SAW strain components in SAW absorptions, magnon-phonon coupling model, SAW transmission model, and Gilbert damping estimation, which includes Refs. [5,14,15,21–23,29,37–40].
- [37] K. Yamamoto, M. Xu, J. Puebla, Y. Otani, and S. Maekawa, Interaction between surface acoustic waves and spin waves in a ferromagnetic thin film, *J. Magn. Magn. Mater.* **545**, 168672 (2022).
- [38] Y. Hwang, J. Puebla, K. Kondou, C. S. Muñoz, and Y. Otani, Nonlinear acoustic spin pumping caused by temperature-dependent frequency shifts of surface acoustic waves, *J. Phys. Soc. Jpn.* **92**, 094702 (2023).
- [39] M. Tarequzzaman, A. S. Jenkins, T. Bohnert, J. Borne, L. Martins, E. Paz, R. Ferreira, and P. P. Freitas, Broadband voltage rectifier induced by linear bias dependence in  $\text{CoFeB/MgO}$  magnetic tunnel junctions, *Appl. Phys. Lett.* **112**, 252401 (2018).
- [40] K. Yamamoto, W. Yu, T. Yu, J. Puebla, M. Xu, S. Maekawa, and G. Bauer, On-chip coherent transduction between magnons and acoustic phonons in cavity magnomechanics, *J. Phys. Soc. Jpn.* **89**, 113702 (2020).



- [41] J. Puebla, M. Xu, B. Rana, K. Yamamoto, S. Maekawa, and Y. Otani, Acoustic ferromagnetic resonance and spin pumping induced by surface acoustic waves, *J. Phys. D* **53**, 264002 (2020).
- [42] T. P. Lyons, J. Puebla, K. Yamamoto, R. S. Deacon, Y. Hwang, K. Ishibashi, S. Maekawa, and Y. Otani, Acoustically driven magnon-phonon coupling in a layered anti-ferromagnet, *Phys. Rev. Lett.* **131**, 196701 (2023).
- [43] M. Ito, S. Ono, H. Fukui, K. Kogirima, N. Maki, T. Hikage, T. Kato, T. Ohkochi, A. Yamaguchi, M. Shima, and K. Yamada, Uniaxial in-plane magnetic anisotropy mechanism in Ni, Fe, and Ni-Fe alloy films deposited on single crystal Y-cut  $128^\circ$  LiNbO<sub>3</sub> using magnetron sputtering, *J. Magn. Magn. Mater.* **564**, 170177 (2022).
- [44] S. W. Sun and R. C. O'Handley, Surface magnetoelastic coupling, *Phys. Rev. Lett.* **66**, 2798 (1991).
- [45] O. M. Chumak, A. Pacewicz, A. Lynnyk, B. Salski, T. Yamamoto, T. Seki, J. Z. Domagala, H. Głowiński, K. Takanashi, L. T. Baczewski, H. Szymczak, and A. Napiórek, Magnetoelastic interactions and magnetic damping in Co<sub>2</sub>Fe<sub>0.4</sub>Mn<sub>0.6</sub>Si and Co<sub>2</sub>FeGa<sub>0.5</sub>Ge<sub>0.5</sub> Heusler alloys thin films for spintronic applications, *Sci. Rep.* **11**, 7608 (2021).
- [46] P. G. Gowtham, G. M. Stiehl, D. C. Ralph, and R. A. Buhrman, Thickness-dependent magnetoelasticity and its effects on perpendicular magnetic anisotropy in Ta/CoFeB/MgO thin films, *Phys. Rev. B* **93**, 024404 (2016).
- [47] M.-A. Lemonde, S. Meesala, A. Sipahigil, M. J. A. Schuetz, M. D. Lukin, M. Loncar, and P. Rabl, Phonon networks with silicon-vacancy centers in diamond waveguides, *Phys. Rev. Lett.* **120**, 213603 (2018).
- [48] U. von Lüpke, Y. Yang, M. Bild, L. Michaud, M. Fadel, and Y. Chu, Parity measurement in the strong dispersive regime of circuit quantum acoustodynamics, *Nat. Phys.* **18**, 794 (2022).
- [49] M. Bild, M. Fadel, Y. Yang, U. von Lüpke, P. Martin, A. Bruno, and Y. Chu, Schrödinger cat states of a 16-microgram mechanical oscillator, *Science* **380**, 274 (2023).
- [50] M. J. A. Schuetz, E. M. Kessler, G. Giedke, L. M. K. Vandersypen, M. D. Lukin, and J. I. Cirac, Universal Quantum Transducers Based on Surface Acoustic Waves, *Phys. Rev. X* **5**, 031031 (2015).
- [51] J. Chen, K. Yamamoto, J. Zhang, J. Ma, H. Wang, Y. Sun, M. Chen, J. Ma, S. Liu, P. Gao, D. Yu, J.-P. Ansermet, C.-W. Nan, S. Maekawa, and H. Yu, Hybridized propagation of spin waves and surface acoustic waves in a multiferroic-ferromagnetic heterostructure, *Phys. Rev. Appl.* **19**, 024046 (2023).
- [52] J. Holanda, D. S. Maior, A. Azevedo, and S. M. Rezende, Detecting the phonon spin in magnon-phonon conversion experiments, *Nat. Phys.* **14**, 500 (2018).